nature communications

Article

https://doi.org/10.1038/s41467-025-57963-8

Ultrahigh dielectric permittivity in $Hf_{0.5}Zr_{0.5}O_2$ thin-film capacitors

Received: 27 November 2024

Accepted: 8 March 2025

Wen Di Zhang [1], **Zi Zheng Song** [2,3], **Shu Qi Tang** [1], **Jin Chen Wei** [1], **Yan Cheng** [4], **Bing Li** [5], **Shi You Chen** [1], **Zi Bin Chen** [2,3] & **An Quan Jiang** [1,6]

The ever-shrinking electrostatic capacitor, which is capable of storing substantial quantities of electrical charge, has found widespread applications in high-storage-density dynamic random access memory and energy-efficient complementary metal-oxide-semiconductor devices. Despite the high energy storage densities (133–152 J/cm^3) and efficiencies (75–90%) that have been realized using relaxor ferroelectric thick films, low-permittivity interfacial layers in the ultrathin films have caused the overall permittivity to be one to two orders of magnitude lower than expected. However, innovative use of complementary metal-oxide-semiconductor-compatible HfO_2-based materials with high permittivities (~52) could enable integration of these capacitors into few-nanometre-scale devices. This study reports an ultrahigh dielectric permittivity of 921, stored charge density of 349 μC/cm^2, and energy density of 584 J/cm^3 with nearly 100% efficiency within near-edge plasma-treated $Hf_{0.5}Zr_{0.5}O_2$ thin-film capacitors when the Hf-based material's ferroelectricity disappears suddenly after polarization fatigue. The ultrahigh dielectric permittivity originates from a distorted orthorhombic phase with ordered oxygen vacancies that enables high-density integration of extremely scaled logic and memory devices for low-voltage applications.

As the lateral dimensions of advanced transistors continue to be scaled down, increased gate capacitance becomes an essential requirement to maintain gate control over the channel and reduce operating voltages for low energy consumption[1]. Traditional scaling methods involve reducing the SiO_2 gate thickness but lead to undesirable leakage, mobility degradation, and reliability issues. Consequently, the efforts to scale complementary metal-oxide-semiconductor (CMOS) devices down to sub-10-nm technologies are focused on the use of high-dielectric-permittivity gate materials to replace SiO_2 and thus realize higher equivalent oxide thicknesses and capacitances (proportional to the dielectric permittivity) to mitigate short-channel effects[2]. Although relaxor ferroelectrics have demonstrated high energy storage densities (133–152 J/cm^3) and efficiencies (75–90%)[3,4], the presence of low-permittivity interfacial layers close to electrodes in thin films could destabilize their ferroelectric states[5–12], causing the overall permittivity to be one to two orders of magnitude lower than expected[7,9,10].

Atomic-layer deposition (ALD) of HfO_2-based thin films, which have high permittivities of 16–70 and ferroelectric polarizations of 17–50 μC/cm^2[13–22], can provide a viable solution to these challenges. The ALD technique offers the advantages of low-temperature synthesis and conformal growth in three-dimensional structures on silicon surfaces, thereby circumventing the high temperature requirements for deposition of ferroelectric perovskite oxides. This has led to applications in

---

[1]School of Microelectronics, Fudan University, Shanghai, China. [2]State Key Laboratory of Ultra-precision Machining Technology, Department of Industrial and Systems Engineering, The Hong Kong Polytechnic University, Hong Kong, China. [3]Research Institute for Advanced Manufacturing, Department of Industrial and Systems Engineering, The Hong Kong Polytechnic University, Hong Kong, China. [4]Key Laboratory of Polar Materials and Devices (MOE), Department of Electronics, East China Normal University, Shanghai, China. [5]School of Life Science and Technology, ShanghaiTech University, Shanghai, China. [6]Shanghai Frontiers Science Research Base of Intelligent Optoelectronics and Perception, Institute of Optoelectronics, Fudan University, Shanghai, China.
e-mail: chensy@fudan.edu.cn; zi-bin.chen@polyu.edu.hk; aqjiang@fudan.edu.cn

volatile/nonvolatile high-storage-density memories and extremely size-scaled CMOS devices for use at low operating voltages[1,13,23,24].

Various approaches have been found to improve the dielectric and ferroelectric properties of HfO_2-based thin films[25–27]. He ion implantation with doses of 5×10^{16}–10^{17} ions/cm^2 can increase the remanent piezoresponse and polarization significantly[28]. HfO_2-ZrO_2 thin films with compositions engineered to be near the antiferroelectric phase transition exhibit a high storage density of 115 J/cm^3 upon nonlinear and hysteretic changes in their dielectric permittivity from 35 to 140 during polar-to-nonpolar phase transitions[29]. These approaches to defect engineering and the antiferroelectric phase transition have driven major efforts to minimize the voltage-dependent dielectric nonlinearity and hysteresis, in addition to increasing the dielectric permittivity[30,31]. This is essential because dielectric nonlinearity and hysteresis can result in the hysteretic field-effect currents in CMOS devices with respect to the rising/falling of gate voltages and also increase the energy consumption of storage devices.

Here we report an oxygen-vacancy-implanted $Hf_{0.5}Zr_{0.5}O_2$ (HZO) thin-film capacitor that shows a dramatic increase in dielectric permittivity of $\varepsilon = \varepsilon' - i\varepsilon''$, where ε' and ε'' are the real and imaginary parts, respectively. Advanced structural characterization shows that an oxygen vacancy-ordered structure is introduced into the polar $Pca2_1$ phase during bipolar high electric-field cycling that enhances the ferroelectric-to-paraelectric transition and results in an ultrahigh dielectric permittivity (~921) that is independent of the applied voltage. This discovery represents a significant advancement for the high-density integration of memory, logic and energy storage devices with low energy consumption.

Results

Ultrahigh dielectric permittivity

The p-Si/TiN (40 nm)/HZO (10 nm)/TiN (5 nm)/W (50 nm) thin-film capacitors were prepared using low-temperature ALD on silicon substrates (Methods and Supplementary Fig. S1a–c). Subsequent O_2 and SF_6 plasma treatments were performed beyond the top electrode areas before and after crystallization of the amorphous HZO, giving samples that were numbered 1 and 2, respectively (Supplementary Fig. S1a, b). X-ray reflection (XRR) analysis indicated an HZO film thickness of 10 nm (Supplementary Fig. S2a, b). Synchrotron grazing-incidence X-ray diffraction (XRD) patterns revealed a mixture of orthorhombic (*O*, *Pca*2_1), tetragonal (*T*, *P*4_2*/nmc*), and monoclinic (*M*, *P*2_1*/c*) phases within the crystallized HZO with area ratios of 0.70:0.21:0.09 for *O* (111), *T* (011), and *M* (111) reflections (Supplementary Fig. S2c). The measured energy dispersive spectrum (EDS) of the film shows a strict Zr:Hf ratio of 1:1 (Supplementary Fig. S3). X-ray photoelectron spectroscopy (XPS) spectra indicate the coexistence of lattice oxygen and non-lattice oxygen in both the ion-implanted amorphous and crystallized HZO, with the former exhibiting a 16% higher content of non-lattice oxygen (Supplementary Fig. S4a–f), suggesting a greater presence of oxygen vacancies near the edge region of the capacitor (Sample 1). The planar capacitor length (l) was determined for each single device from scanning electron microscopy (SEM) images of the top electrodes (Supplementary Fig. S5). Characteristic current density-electric field curves show that all capacitors are insulating (Supplementary Fig. S6a). A stopping and range of ions in matter (SRIM) simulation showed that ~42% more oxygen vacancies were generated within Sample 1 than within Sample 2 after the near-edge plasma treatment outside the top electrode areas (Supplementary Fig. S1c). These oxygen vacancies ($V_O^{\cdot\cdot}$) could then diffuse into the inner regions beneath the top electrode areas during final thermal annealing at 550 °C for 30 s (Supplementary Fig. S1a, b)[28]. This penetration region is anticipated to have a characteristic length denoted by r_0, as depicted in the inset of Fig. 1a; this length is postulated to exert a considerable influence on the dielectric properties, and this effect will be explored in subsequent discussions.

Figure 1a displays the electrode area (S) dependences of the small-signal capacitance (C) of Samples 1 and 2 at 1 MHz after near-edge ion implantations. The *C-S* dependence is linear for Sample 2, as demonstrated by solid-line data fitting when $\varepsilon' = 32$, but it is nonlinear for Sample 1 because of the presence of higher oxygen vacancies within the edging areas. After solid-line fitting of the nonlinear *C-S* plot, we derived $r_0 = 150$ nm (see Methods). Consequently, the ensuing electrical characterization and the analytical discourse will concentrate primarily on the nonlinear size-scaling effect in Sample 1, except where noted otherwise.

Figure 1b, c illustrates the frequency (f) dependences of ε' and the loss tangent (tanδ) for Sample 1. ε' shows a step-like enhancement when $f < 10$ kHz but increases nonlinearly from 32 to 75 at 1 MHz upon reduction of l from 32.3 to 4.39 μm in Fig. 1b. Correspondingly, increasing dielectric loss peaks appear between 10 and 20 kHz in Fig. 1c. Subsequent measurements of the dielectric displacement −electric field (*D-E*) hysteresis loops in Fig. 1d (Supplementary Fig. S6b–e) show progressive reduction of the remanent polarization (P_r) from 16 to 6.5 μC/cm^2 during shrinkage of l from 9.05 to 4.35 μm. However, this size-dependent effect is negligible in Sample 2, apart from the disappearance of the dielectric loss peak (Supplementary Fig. S7a, b). The enhanced dielectric permittivity observed alongside the reduction of P_r in Sample 1 appears to originate from the increased volume fraction of near-edge implanted areas in the downscaled capacitors, where numerous superparaelectric regions exist[4]. Dipole orientations within these regions can follow an oscillating electric field (E_{osc}) reversibly during the periods above their relaxation times, enhancing ε' at frequencies below 20 kHz during the generation of the resonant dielectric loss peaks in Fig. 1c.

Following application of square pulses with bipolar voltages/durations of ±4 V/500 ns to the capacitors when $4.35\ \mu m \le l \le 5.42\ \mu m$, the ferroelectricity disappears abruptly (with P_r approaching 0) after fatigue numbers of 2.07×10^7–6.62×10^7, as illustrated in Fig. 1e. This disappearance is accompanied by the emergence of linear *D-E* loops in Fig. 1f. From the slopes of these linear loops, we estimated ultrahigh dielectric permittivities of 642–921 at 1 MHz. The subtle study of the *D-E* loops near the transitional switching cycles shows that the ultrahigh ε' transition occurs earlier before the ferroelectric-to-paraelectric phase transition (Supplementary Fig. S6c–e). Otherwise, dielectric breakdown occurs before the ultrahigh ε' transition for capacitors where $l \ge 9.05\ \mu m$ (Fig. 1e).

After fatigue, we calculated ε' at different frequencies separately based on independent measurements of the small-signal capacitance at various l, as depicted in Fig. 2a, revealing the disappearance of the dielectric loss peaks between 10 and 20 kHz. At 1 MHz, ε' increases to 921 when $l = 4.39$ μm, showing precise agreement with the value estimated from the slope of the linear *D-E* loop in Fig. 1f and yielding a substantial storage charge density of 295 μC/cm^2 and energy storage density of 566 J/cm^2 with nearly 100% efficiency under a high applied electric field of 4 MV/cm (Supplementary Fig. S8a, b). The ultrahigh-ε' phase remains stable over a laboratory time of more than two years, even after cooling/heating of Sample 1 between 85 and 300 K. Figure 2b, c illustrates the temperature (T) evolutions of the dielectric response and *D-E* hysteresis loop, respectively. ε' decreases almost linearly versus T during cooling in Fig. 2b, thus approximately matching the estimates based on the slopes of the linear *D-E* loops in Fig. 2c (Supplementary Fig. S9a–d). Both ε' and tanδ remain unchanged versus amplitudes of E_{osc} from 20 kV/cm to 0.8 MV/cm and E from −2 to 2 MV/cm (Supplementary Fig. S10a–c). The stored charge density after fatigue increases by 10 times at both low and high frequencies (Supplementary Fig. S8c, d), enabling 100 μC/cm^2 to be stored at an operating voltage/time of 1.2 V/50 ns in the dynamic random access memory (DRAM) at cycle numbers of more than 10^{12} without inducing dielectric breakdown (Fig. 2d). The shortest operation time here is limited by the circuit *RC* time of 14 ns,

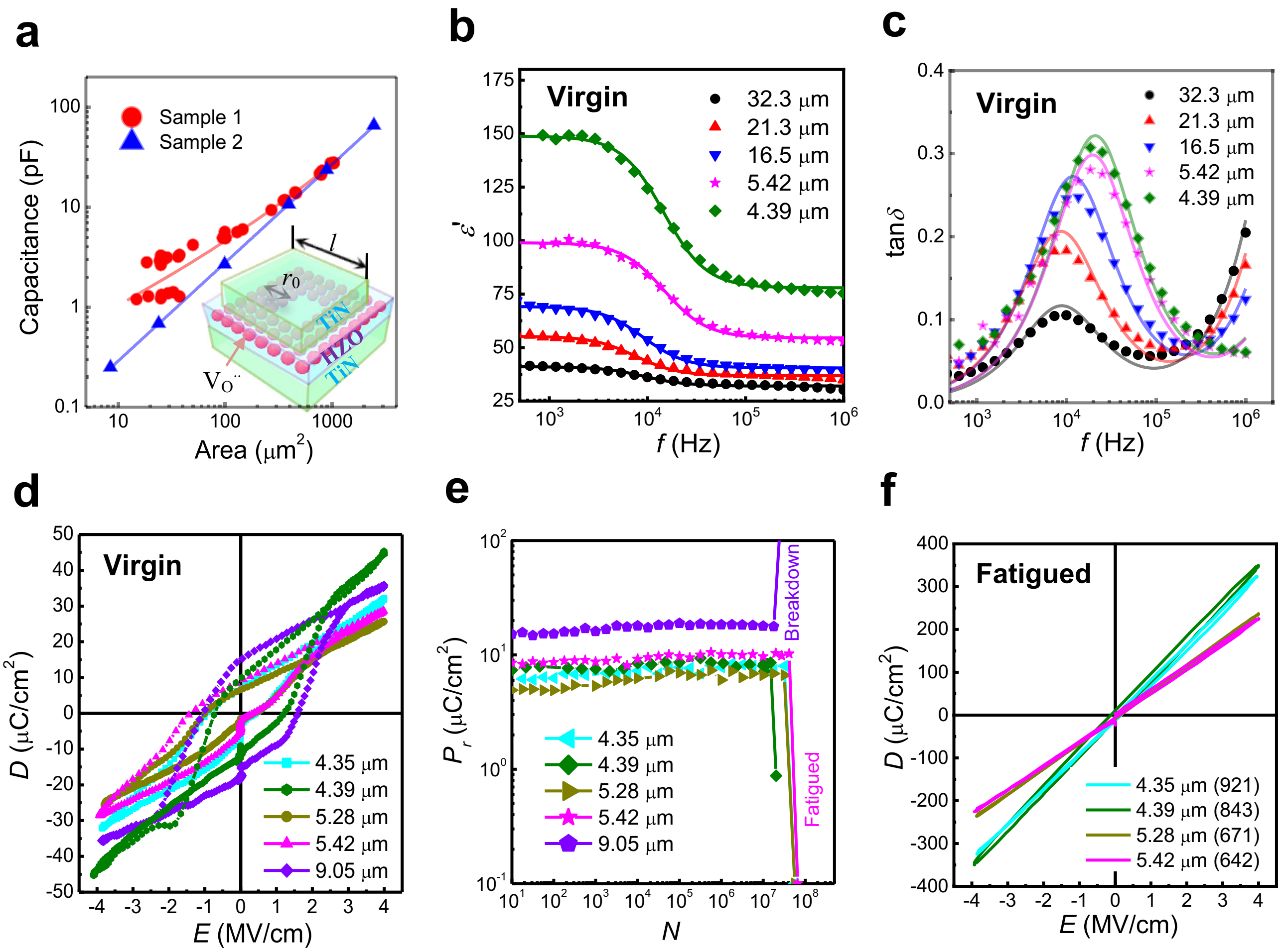

Fig. 1 | Dielectric permittivities of size-scaled capacitors. a Area dependences of the capacitance at 1 MHz for Samples 1 and 2. The solid lines represent the best fit for the data when considering the edging-area contribution under the top electrodes in the geometries illustrated in the inset based on the assumptions of $r_0 = 150$ nm and 0 nm, respectively. The large deviation of data from the red-line fit is due to the variation of ion implantation across different areas of the film. **b**, **c** Frequency dependences of ε′ and tanδ for virgin HZO capacitors of various sizes (Sample 1). The solid lines represent data fittings according to Eq. (4). **d** *D-E* hysteresis loops for the size-scaled virgin capacitors when characterized at 1 MHz. **e** Cycling number dependences of the remanent polarization values of the size-scaled capacitors when using square pulses of ±4 V/500 ns at a repeat frequency of 1 MHz. **f** *D-E* hysteresis loops at 1 MHz for the size-scaled capacitors after fatigue, where the parenthetic values of ε′ are estimated from the slopes of the loops.

which is hopefully shortened again in the future through the improvement of the TiN electrode conduction (Supplementary Fig. S11a–c). This record-breaking ε′ value is the highest reported among pure and doped HfO_2 thin films (Fig. 2e), thus making it extremely attractive for high-density DRAM and CMOS applications[1,23]. In contrast, Sample 2, which underwent plasma treatment after HZO crystallization, exhibits no such ultrahigh-ε′ transition (Supplementary Fig. S12a, b).

The synchrotron Laue micro-diffraction measurements of the size-scaled capacitors (Sample 1) indicate continuous weakening in the intensity of the *O* (111) reflection as the lateral dimension of the capacitor decreases, particularly when the illuminated light spot covers an increasing edge area (Supplementary Fig. S13a–c). Figure 2f shows the Laue micro-diffractions of both virgin and fatigued areas, derived from Gauss functional fittings of the nearby *O* (111) /*T* (011) reflections from the 4.35 μm-long fatigued capacitor (Supplementary Fig. S13a, c). The *O* (111) peak diminishes further after fatigue and shifts slightly towards a lower angle (indicative of lattice expansion), with a significant increase in width from 0.089° to 0.52°. The peak broadening implies the presence of defect structures and alterations in the polar regions within the *O*-phase after fatigue[32–34].

Phase structure

To understand the structural origins of the ultrahigh-ε′ transition, atomic-scale microstructural characterizations of Sample 1 before and after fatigue were conducted using scanning transmission electron microscopy (STEM)−high angle annular dark-field (HAADF) and STEM-integrated differential phase contrast (iDPC) imaging techniques. Although both STEM-HAADF and STEM-iDPC image contrasts are sensitive to atomic numbers, STEM-iDPC images offer better contrast for lighter elements, e.g., oxygen in HZO, thus making it easy to identify oxygen vacancies by differentiating the contrast change across the different oxygen columns within the ferroelectric *O*-phase grains. Figure 3a shows a low-magnification STEM-HAADF image of the virgin Sample 1. In the central region when $r_0 > 150$ nm (Fig. 3b), all oxygen columns exhibit similar intensities (Fig. 3d), demonstrating zero oxygen vacancies across these areas. In stark contrast, within the near-edge regions when $r_0 < 150$ nm (Fig. 3c), significant contrast variations were found across the oxygen columns (Fig. 3e), indicating the existence of large numbers of oxygen vacancies within these areas. This observation confirms the presence of a near-edge oxygen vacancy penetration zone (r_0) caused by the pre-crystallization plasma treatment.

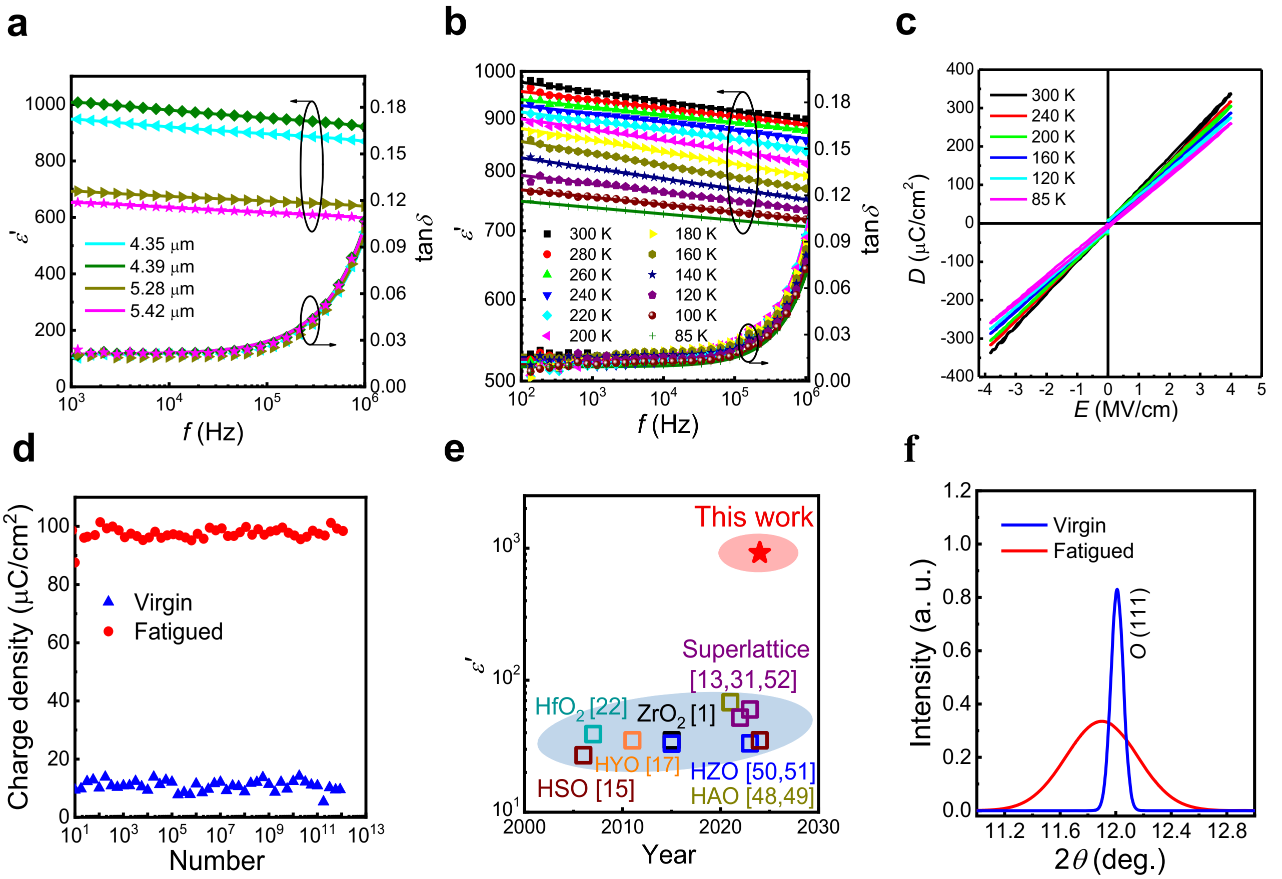

Fig. 2 | Ultrahigh dielectric permittivities. a Frequency dependences of ε' and tanδ when $E_{osc} = 50$ kV/cm for the size-scaled capacitors after the occurrence of polarization fatigue. Larger capacitor sizes generally result in smaller values of ε'. The solid lines represent data fittings according to Eqs. (5) and (6). **b** Frequency dependences of the dielectric permittivity and loss tangent at various temperatures for the 4.39-μm-long fatigued capacitor. The solid lines represent data fittings according to Eqs. (5) and (6). **c** *D-E* hysteresis loops at 252 kHz for the 4.39-μm-long fatigued capacitor at different temperatures. **d** Cycling number dependences of the stored charge density within the 4.39-μm-long virgin/fatigued capacitors under application of unipolar square pulses with voltage/width characteristics of 1.2 V/50 ns with a repetition frequency of 10 MHz at room temperature. The charge density increases by 10 times after fatigue. **e** Comparison of the ultrahigh dielectric permittivity realized in this work with the corresponding values for the pure ZrO_2 and HfO_2[21,23], Al-doped HfO_2 (HAO)[55,56], Si-doped HfO_2 (HSO)[14], Y-doped HfO_2 (HYO)[16], Zr-doped HfO_2 (HZO)[57,58], and HfO_2-ZrO_2 superlattices[13,29,59] reported previously in the literature. **f** Synchrotron Laue micro-diffractions of the *O* (111) reflections extracted from the virgin and fatigued areas nearby a 4.35 μm-long capacitor at a wavelength of 0.6209 Å (Supplementary Fig. S13a–c).

The ferroelectricity of HZO originates from the $Pca2_1$ phase[15–22]. The atomic structure of HZO changes substantially after fatigue. Figure 3f shows a typical atomic structure for the [010]-$Pca2_1$ phase after fatigue, with a corresponding atomic model shown in the top-left corner. In contrast to the perfect structure before fatigue, where two consecutive oxygen columns along the $[10\bar{1}]$ and $[\bar{1}0\bar{1}]$ directions should contain the same number of oxygen atoms with identical contrasts, the new structure after fatigue interestingly exhibits regularly alternating intensity fluctuations within the oxygen columns. Figure 3g, h show the profiles of two intensity lines when scanned along the $[10\bar{1}]$ and $[\bar{1}0\bar{1}]$ directions indicated in Fig. 3f, respectively. The regularly modulated intensities of the O columns, which are lower than the reference full-O intensity (represented by the dashed lines), imply the periodic appearance of oxygen vacancies at the O_2, O_4, and O_5 sites. Therefore, all oxygen vacancies were ordered at either the O_2 and O_5 sites in Fig. 3g or the O_4 sites in Fig. 3h during formation of the new structure, denoted by $Pca2_1'$, unlike the randomly distributed oxygen vacancies in the virgin Sample 1 (Fig. 3e). To exclude microstructural contingencies, we scanned seven more continuous atom column lines in the fatigued capacitor, verifying that all vacancies were located in an orderly manner at the O_2, O_4, O_5 and O_7 sites (Supplementary Fig. S14a–c). In addition, we imaged the O columns in another [001] orientation of the $Pca2_1'$ phase and confirmed the presence of the same ordered $V_O^{\cdot\cdot}$ structure along a different viewing direction (Supplementary Figs. S15a–c and S16).

The presence of ordered oxygen vacancies significantly enhances the number of polar regions in the *O* phase. The STEM-DPC imaging technique was employed to observe these polar regions, as illustrated in Supplementary Fig. S17. Different colors in the color wheel represent the directions of the internal electric fields in the examined areas. In contrast to the virgin sample, where the bulk domain has a uniform internal electric field, the fatigued sample exhibits highly segmented polar regions with random directions of internal electric fields. These segmented polar regions could corroborate our observation of the broadening in the *O*-phase peak of the Laue micro-diffraction patterns (Fig. 2f), which are believed to play a critical role in determining dielectric properties of the fatigued samples.

Discussion

The dielectric responses of the dipoles within the $V_O^{\cdot\cdot}$-implanted near-edge areas in Sample 1 can be described using the classical Debye equation[35]. After solid-line fitting of the data in Fig. 1b, c (see Methods), we derived a Debye relaxation time of τ that decreases from 18 to 7.8 μs with the lateral shrinkage of l from 32.3 to 4.39 μm in Fig. 1c. Similar dielectric dispersion has been observed in etched lead zirconate titanate (PZT) capacitors, where the relaxation time τ exhibits an

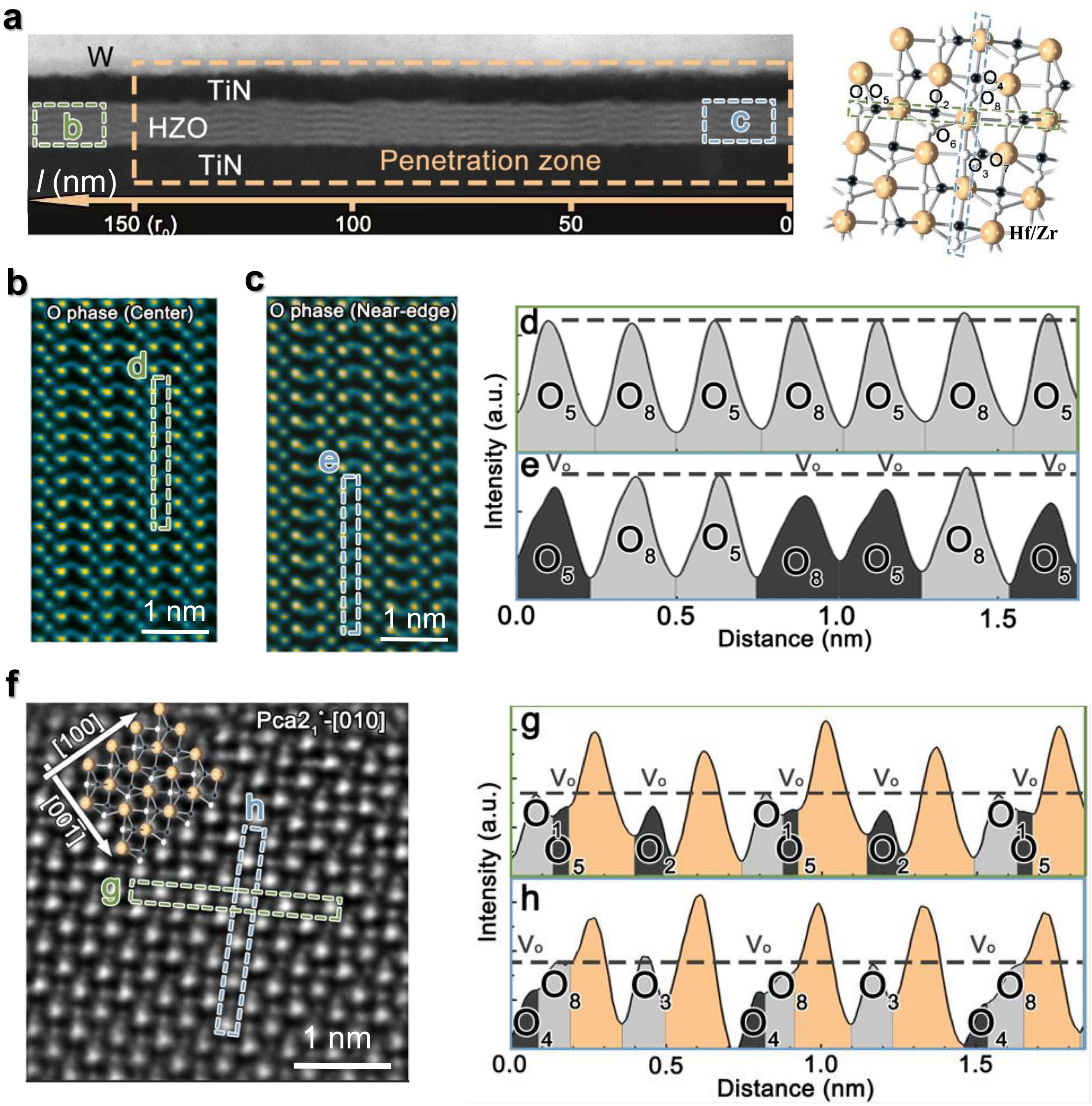

Fig. 3 | Phase structures (before and after fatigue). **a** Low-magnification cross-sectional STEM-HAADF image of virgin HZO thin film (left panel). The framed yellow dashed rectangle is the oxygen vacancy penetration zone (~150 nm). The right-hand panel shows the simulated atomic structure for the [010]-*Pca*2_1 phase. **b**, **c** STEM-iDPC images of the *O* phases beyond and within the penetration zone framed in **a**, respectively. **d**, **e** Line scans over the rows of the oxygen columns framed in **b**, **c**, respectively. The dashed lines represent the intensities of the reference fully O-occupied columns, and the peak intensities that are lower than the reference line in **e** indicate the appearance of random oxygen vacancies at the O_5 and O_8 sites. **f** STEM-iDPC image of the [010]-oriented *Pca*2_1′ phase after fatigue. The inset in the top-left corner shows the simulation of this phase. **g**, **h** Two line scans of the atomic columns within the dashed rectangles framed in (**f**). Periodic changes in the oxygen intensities that deviate from the reference full-O dashed lines at the O_2, O_4 and O_5 sites consistently implies the appearance of ordered oxygen vacancies when measured along two different ([$10\bar{1}$]and[$\bar{1}0\bar{1}$]) directions.

exponential relationship with the perimeter[36,37]. According to the model proposed by Dawber et al.[36], inhomogeneous domain nucleation occurs at imperfections near the edges of the etched PZT capacitors, with domain-wall motion being restricted by viscous drag resulting from the coupling of the domain wall to acoustic phonons. Consequently, τ represents the time required for domain walls to propagate from the perimeter to the center of the capacitor. Given that our HZO film is continuous, we propose that similar domain nucleation could occur near the edge regions of each capacitor, which are enriched with oxygen vacancies. After polarization fatigue, the Debye relaxation was absent from Fig. 2a. Instead, a universal law can be used to describe the dielectric dispersion (see Methods)[35], as evidenced by solid-line fitting of the data in Fig. 2a, b. This could reflect the redistribution of the oxygen vacancies.

Generally, the ferroelectric-to-paraelectric phase transition is associated with the emergence of a giant dielectric constant ε' at the Curie point, a phenomenon resulting from the collapse of ferroelectric macrodomains and the formation of multiple transitional polar regions prior to the complete loss of ferroelectricity[7,11,33–35,38–40]. Domain nucleation within the polar regions, hindered by viscous drag[36], is characterized by low energy, allowing dipole polarizations within these regions to reversibly follow the E_{osc}, thereby significantly

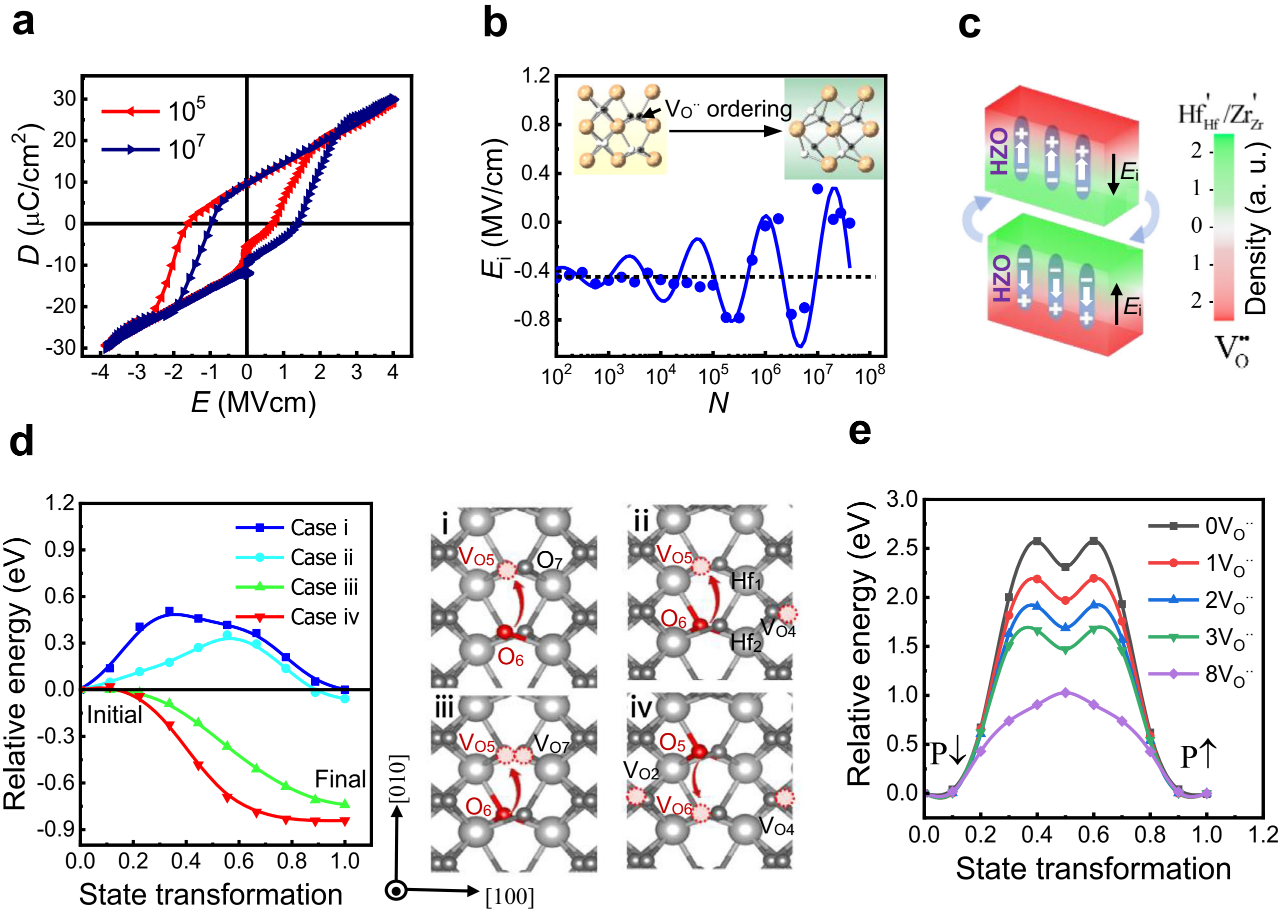

Fig. 4 | Oxygen vacancy ordering process and simulations. **a**, **b** Cycling number dependences of the *D*-*E* hysteresis loop and the imprint field for the 5.42 μm-long HZO capacitor when using square fatigue pulses of ±4 V/500 ns at a repetition frequency of 1 MHz. The solid line in **b** represents the fit of an oscillating imprint field according to Eq. (1) that accompanies the $V_O^{\cdot\cdot}$ ordering illustrated in the inset figures. **c** Schematic of the preferred $V_O^{\cdot\cdot}$ accumulation near the top/bottom electrodes during fatigue that is interdependent on the E_i direction (thin arrows). The built-up internal field caused by the $V_O^{\cdot\cdot}$ accumulation contradicts E_i and changes the dipole orientation (thick arrows). **d** Minimum energy paths for the O-anion movement within the (001) crystal plane in a 96-atom supercell for Cases i–iv. The dotted balls represent oxygen vacancies, the red balls represent the displaced oxygen anions, and the arrows indicate the movement directions. **e** Minimum energy paths for bipolar polarization switching with different numbers of three-coordinated oxygen vacancies within a 96-atom supercell. The arrows indicate the polarization (P) orientations in the initial and final states.

enhancing ε'[4,33,34,39,40]. To examine these polar regions in the virgin Sample 1, we extracted the dielectric permittivities $\varepsilon'_{central}$ and ε'_{edge} near the central and near-edge regions, respectively, from measurements of the ε'-E_{osc} dependences at various *l*, and found that $\varepsilon'_{central} \propto \beta E_{osc}^2$ ($\beta > 0$, power law) and $\varepsilon'_{edge} \propto \alpha E_{osc}$ ($\alpha < 0$, Rayleigh law), where α and β are constants representing irreversible dielectric contributions stemming from domain-wall pinning and depinning, respectively (Supplementary Fig. S18a–c). These phenomena are attributed to the presence of homogeneously and inhomogeneously distributed oxygen vacancies in the two cases[38,39]. The negative α value indicates the superparaelectricity of the near-edge polar regions[38], where the dipoles can follow the E_{osc} oscillation when $f < \tau^{-1}$ [40].

To explore the $V_O^{\cdot\cdot}$ ordering process during fatigue, we inspected the *D*-*E* hysteresis loops at various fatigue numbers (*N*) (Fig. 4a, Supplementary Fig. S19a–f). From these measurements, we extracted the log*N* dependence of the imprint field (E_i), i.e., the shift in an asymmetric *D*-*E* hysteresis loop along the *E*-axis (Fig. 4b, Supplementary Fig. S19a, c). $|E_i|$ strengthens versus log*N* in a wave-like manner to obey the following equation:

$$E_i = E_0 + E_A \log^2 N \cdot \sin\frac{2\pi(\log N - \log N_0)}{\lambda} \qquad (1)$$

until the ultrahigh-ε' transition occurs; here, E_0 and E_A are the initial value and amplitude of the oscillating imprint field, respectively, N_0 is the initial number, and λ is the periodicity. Analysis of the solid-line fitting to the capacitor data when $l = 5.42$ μm in Fig. 4b reveals that $\lambda = 1.3$ increases to 3.0 upon reduction of *l* to 4.39 μm (Supplementary Fig. S19a). This is distinct from most other ferroelectric thin films and Sample 2, where no E_i oscillations occur (Supplementary Fig. S12a)[41].

The intrinsic E_i oscillation physics could be correlated with the $V_O^{\cdot\cdot}$ ordering process within HZO (Fig. 4c). Given the oxygen vacancies and the structural disorder introduced via plasma treatment of the amorphous HZO[26,27], the near-edge regions in virgin Sample 1 contain rich polar regions. When the dipoles within the near-edge polar regions are presumed to be polarized and pointing towards the top electrode (upper panel, Fig. 4c), it can generate an opposite depolarization field E_i[42]. When the fatigue periodicity (1 μs) falls below the Debye relaxation time (7.8–18 μs), these dipole orientations cannot synchronize with the cycling fatigue fields, unless a preferential accumulation of oxygen vacancies occurs near the bottom electrode, leaving uncompensated reduced metal ions (Hf'_{Hf}/Zr'_{Zr}) behind near the top electrode[43]. The preferential $V_O^{\cdot\cdot}$ accumulation builds up an opposing electric field to contradict E_i. When the opposing field is strong enough, the dipoles are reversed and point towards the bottom electrode (lower panel, Fig. 4c), changing the E_i direction to promote $V_O^{\cdot\cdot}$ accumulation towards the top electrode. Throughout the fatigue cycling process, this behavior was repeated periodically as a function of log*N* within the ferroelectric *O*-phase grains until the $Pca2_1'$ phase transition occurred, which resulted in collapse of the ferroelectric domains and a significant increase in the polar regions. In this sense, the $V_O^{\cdot\cdot}$ accumulation process accelerates with increasing $|E_i - E_0|$. When $|E_i - E_0|$ is larger than a threshold field, for example, 0.72 MV/cm in Fig. 4b, the $Pca2_1 \rightarrow Pca2_1'$ phase transition occurs, and $2P_r$ drops abruptly in Fig. 1e. The oscillating $V_O^{\cdot\cdot}$ accumulation process toward top/bottom electrodes seem to be a collective behavior, and is intrigued by the near-edge implanted $V_O^{\cdot\cdot}$. For a larger capacitor, the ratio of near-edge implanting area is lower, and the $V_O^{\cdot\cdot}$ accumulation process is slow (Supplementary Fig. S19a, d). Therefore, dielectric breakdown occurs earlier before the ultrahigh ε' transition. For a smaller capacitor, the ratio of near-edge implanting area increases, which accelerates the $V_O^{\cdot\cdot}$ accumulation process and thus ultrahigh ε' transition before the occurrence of dielectric breakdown in Fig. 1e. Once the ferroelectric polarization disappears within the HZO, there is no dielectric breakdown with the fatigue number higher than 10^{12} (Supplementary Fig. S19e–g).

To gain further understanding of the periodic arrangement of the oxygen vacancies located at the O_2, O_4, O_5, and O_7 sites within the defective $Pca2_1'$ phase, we performed first-principles calculations of the state-transformation energy barrier in a 96-atom supercell (Supplementary Fig. S16a, b). Figure 4d shows the minimum energy path (MEP) of the O-anion movement from a three-coordinated O_6 site to V_{O5}. On the introduction of one V_{O5} in Case I, the O moving energy barrier is as low as 0.51 eV because of partial nonstoichiometry in the lattice and dangling bonds at cation atoms. On the input of another V_{O4} in Case II or another V_{O7} in Case III, the MEP barrier decreases further to 0.35 eV in the former case but completely disappears in the latter case. During oxygen vacancy ordering at the O_2, O_4, and O_5 sites observed in Fig. 3g, h, the O moving MEP barrier from a three-coordinated O_5 site to V_{O6} disappears on the input of additional V_{O2} and V_{O4} in Case IV, where the transformation-state energy is the lowest. This vanished energy barrier energetically favors spontaneous and directional O movement during $V_O^{\cdot\cdot}$ ordering, thus resulting in a large dielectric response under an applied E_{osc}. The decreasing energy barrier can be understood based on the lattice strain relaxation caused by the missing O atoms. In the absence of the four-coordinated O_4 atom, the Hf_1 and Hf_2 atoms distort slightly toward the O_4 site, which expands the movement path and weakens the interaction with the three-coordinated O anions. Furthermore, the Hf_1 atom has a stronger tendency to bind with the O atom than Hf_2 because it loses one more bound O atom, leading to much lower total energy after the state transformation.

Because the calculated transition level for all oxygen vacancies is quite close to the conduction band minimum[44], we assumed that all oxygen vacancies were charged in a +2 state. Note that the spontaneous polarization of HZO originates from O displacements at the three-coordinated O_5 and O_7 sites. The calculated state-transformation energy barrier between the two opposite polarization states at these sites is also sensitive to the number of oxygen vacancies[45], as illustrated in Fig. 4e. In the virgin state without $V_O^{\cdot\cdot}$, the energy barrier reaches as high as 2.57 eV. On the introduction of 1–8 three-coordinated oxygen vacancies into the 96-atom supercell, the energy barrier decreases progressively to 1.03 eV, i.e., a loss of 12.5% of the O atoms leads to an ~60% reduction in the coercive field. During $V_O^{\cdot\cdot}$ ordering, more oxygen vacancies would be involved, thus lowering the energy barrier further and causing the formation of multiple polar regions, where the dipolar orientations can follow the E_{osc} oscillation reversibly.

In summary, we observed enhanced dielectric permittivity after near-edge ion implantation in amorphous HZO thin-film capacitors. After bipolar high electric-field cycling of a few micron-sized capacitors, the ferroelectricity disappears suddenly between fatigue numbers of 2.02×10^7 and 6.62×10^7 during the generation of a voltage-independent and hysteresis-free ultrahigh ε' (598–921 at 1 MHz). High-resolution STEM-iDPC images reveal ordered oxygen vacancies within the principal O-phase grains, forming a new $Pca2_1'$ phase that results in the formation of multiple polar regions and contributes to the ultrahigh dielectric permittivity. First-principles calculations consistently demonstrated progressive reduction of the energy barriers for spontaneous and directional O movements and ferroelectric displacements with the involvement of increasing numbers of oxygen vacancies during ordering. The ultrahigh-ε' transition enables realization of high charge- and energy storage devices and energy-efficient transistors[1,3,16,22,23].

Methods

HZO fabrication

Continuous $Hf_{0.5}Zr_{0.5}O_2$ thin films were grown by ALD (TFS 200, Beneq) at 200 °C on a Si substrate coated with 10-nm-thick TiN bottom electrodes, where hafnium tetrachloride ($HfCl_4$) and zirconium tetrachloride ($ZrCl_4$) precursors were used, with water (H_2O) as the oxidizing reactant and argon (Ar) acting as a purging gas. A 1:1 ratio between the alternately laminated HfO_2 and ZrO_2 atomic layers (~1 nm) was used to set the desired stoichiometry for a deposited film with a total thickness of 10 nm. The film thickness can be determined from XRR using a Cu K_α source (D2, Bruker) and HAADF-STEM (Fig. 3a and Supplementary Fig. S2a, b), and the film compositions can be determined from EDS mapping of alternative Hf and Zr stacking layers (Supplementary Fig. S2c). TiN and W electrode layers were deposited by sputtering (PVD-75, Kurt J. Lesker) at room temperature. The thermal annealing process for Samples 1 and 2 was performed at 550 °C for 30 s in an N_2 atmosphere to enable crystallization of the HZO before and after etching of the top electrodes, respectively (Supplementary Fig. S1a, b). After photoresist layer patterning of the top electrodes using ultraviolet photolithography (NQX4006, Neutronix-Quintel), the top electrodes were etched into square/circular shapes with side lengths/diameters of *l*, respectively, via ion milling using SF_6 and O_2 plasmas with gas flows of 15 and 5 sccm, respectively, at an output power of 50 W for 30 s in a reactive ion etching system (RIE-10NR, Samco, Japan). Near-edge implantation of the oxygen vacancies occurs during etching (Supplementary Fig. S1c). The capacitor dimensions were verified using planar-view SEM (Sigma HD, Zeiss) images (Supplementary Fig. S4). Leakage current-voltage curves were measured using an Agilent B1500A semiconductor analyzer operating in voltage-sweep mode (Supplementary Fig. S5a). The valence states analysis of Zr, O, and Hf within the HZO was performed on an XPS (Thermo Fisher ESCALAB 250Xi) using Al *K*α emission in an energy of 1486.6 eV. After the deconvolution of the XPS spectra (Supplementary Fig. 4Sa–f), it is found that the lattice oxygen and non-lattice oxygen coexist at binding energies of 529.9 eV and 531.2 eV within the ion-implanted crystallized HZO, respectively. Their energies shift by 0.65 eV within the ion-implanted amorphous HZO. From the area integrations of these peaks, we conclude that the non-lattice oxygen content in the latter film increases by 16%.

X-ray diffraction

Synchrotron XRD (Supplementary Fig. S2c) measurements were performed using a grazing-incidence synchrotron radiation source (~1°) at a wavelength of 0.6887 Å located at the Shanghai Synchrotron Radiation Facility. After integration of the *O* (111), *T* (011) and *M* (111) reflections using Gaussian function fitting of their three peaks at $2\theta = 13.51°$, 13.60°, and 13.98°, respectively[46], we calculated their area ratio of 0.70:0.21:0.09 for the TiN-capped HZO thin films, in line with the prediction of the principal *O* phases within both Samples 1 and 2. However, the partial *O* phase transformed into *T* after the removal of the top TiN capping layer[22,46–49]. For understanding of the size-scaling effect on the dielectric permittivities and phase structures, we performed synchrotron Laue micro-diffractions using an ellipsoidal light spot in major and minor axes of 5 and 10 μm at a wavelength of 0.6209 Å, respectively. In consideration of the normally incident light spot larger than the fatigued capacitor, the Laue diffraction from the fatigued area can be obtained in Fig. 2f after the subtraction of the diffraction contributed by the peripheral virgin area when the fatigued area was cutoff after the measurement using a FIB technology (Supplementary Fig. S13a–c).

HAADF-STEM characterization

After electrical characterization, cross-sectional TiN/HZO/TiN specimens were prepared for the HAADF-STEM observations using a FIB technique in the FEI Helios G4 system, including low-pressure polishing processes that were performed at 5 and 2 keV. The samples were then treated in a Gatan 691 precision ion polishing system at energies of 1–0.5 keV to remove any residual contamination and damage from the sample surfaces. STEM experiments were then conducted using a Thermo Fisher Spectra 300 microscope operating at 300 kV with double spherical-aberration (Cs) correctors. HAADF-STEM images were acquired using an annular dark-field image detector that had an inner semi-angle of more than 58 mrad and iDPC images were acquired using a segmented DF detector that had a semi-angle range of 5–23 mrad. The probe convergence semi-angle for the microscope was ~25 mrad. The *O*-phase symmetry seems to be unchanged after fatigue (Figs. 2f and 3f).

Size-scaling effect and dielectric relaxation

The small-signal capacitance and the loss tangent characteristics were measured using a Precision LCR Meter (Agilent E4980A) operating at an AC amplitude of 0.05 V ($E_{\mathrm{osc}} = 50$ kV/cm) within the frequency range from 100 Hz to 1 MHz without the application of the DC bias; these characteristics comprised the capacitances measured from the edging area $4(lr_0 - r_0^2)$ and the central area $(l - 2r_0)^2$ for a square capacitor, as illustrated in the inset in Fig. 1a. After solid-line fitting of the *C-S* plot for Sample 1 in Fig. 1a when the dielectric permittivities of the central area $\varepsilon'_{central} = 921$ and the edge area $\varepsilon'_{edge} = 24$ [13–21], the penetration length r_0 was derived to be 150 nm.

The dielectric relaxation of the defect dipoles within the near-edge areas can be described using the classical Debye equation given by ref. 35

$$\varepsilon(\omega) = \varepsilon_\infty + \frac{\varepsilon_0 - \varepsilon_\infty}{1 + i\varpi\tau}, \tag{2}$$

where τ is relaxation time for the dipoles, and ε_∞ and ε_0 are the dielectric permittivities at the highest and lowest frequencies ($\omega = 2\pi f$), respectively.

The partial oxidation of the TiN top electrode that occurs during thermal crystallization of the HZO thin film leads to the presence of an interfacial layer within the resistance of R_i[48]. After data fitting of the capacitor charging current transients versus time under different applied voltages, we estimated that $R_i = 0.85$ kΩ (Supplementary Fig. S11a); alternatively, we estimated that $R_i = 0.98$ kΩ from the linear current–voltage curve after the occurrence of the dielectric breakdown (Supplementary Fig. S11b, c). When considering a Debye-like capacitor in series with R_i, Eq. (2) should be modified to read:

$$\varepsilon(\omega) = \frac{\varepsilon_0 + i\omega\tau\varepsilon_\infty}{(1 - \omega^2\tau R_i C_0 \varepsilon_\infty) + i\omega\tau} \quad (\tau >> R_i C_0), \tag{3}$$

where $C_0 = \varepsilon_v S/d$, d is the film thickness, and ε_v is the vacuum permittivity. Based on the consideration that $\varepsilon = \varepsilon' - i\varepsilon''$, we calculated

$$\begin{cases} \varepsilon' = \frac{\varepsilon_0\left(1 - \omega^2\tau R_i C_0 \varepsilon_\infty\right) + \omega^2\tau^2\varepsilon_\infty}{\left(1 - \bar{\omega}^2 R_i C_0 \tau\varepsilon_\infty\right)^2 + \bar{\omega}^2\tau^2} \\ \varepsilon'' = \frac{\omega^3\tau^2\varepsilon_\infty^2 R_i C_0 + \left(\varepsilon_0 - \varepsilon_\infty\right)\omega\tau}{\left(1 - \bar{\omega}^2\tau R_i C_0 \varepsilon_\infty\right)^2 + \bar{\omega}^2\tau^2} \\ \tan\delta = \frac{\varepsilon''}{\varepsilon'} \end{cases} \tag{4}$$

After determining the best solid-line fits for the data in Fig. 1b, c, we derived $\tau = 7.8$–18 μs and $R_i = 0.76$ kΩ. After the occurrence of the polarization fatigue shown in Fig. 1e, the Debye relaxation disappears from Fig. 2a, and a universal law can then be used to describe the dielectric dispersion in the following form of ref.[35]

$$\varepsilon(\omega) \propto (i\omega)^{n-1}, \tag{5}$$

where $0 < n \leq 1$. Based on consideration of R_i in series with a universal capacitor[50], we obtain[35]

$$\tan\delta = \omega\tau' + \mathrm{ctan}\frac{n\pi}{2} \tag{6}$$

with the assumption that $n \to 1$, where $\tau' = CR_i$. The solid lines shown in Fig. 2a, c represent the best fits for the data according to Eqs. (5) and (6), from which we derived $n = 0.984$–0.994 and $R_i = 760$–$958\,\Omega$ (Supplementary Fig. S9b).

D-E hysteresis loops

The high-frequency *D-E* hysteresis loops were transformed from the measurements of the domain switching current transients versus time[51]. After the application of negative/positive poling voltages to the top electrode of the HZO capacitor, with the bottom electrode remaining grounded, the domain switching/nonswitching currents through an in-series resistor R under applied positive switching voltages were observed using an 8 GHz High Definition Oscilloscope (WavePro 804HD, LeCroy, USA) with 12-bit voltage resolution. Through time integration of the current transient, we calculated the charge density and/or the polarization. Square switching pulses were supplied using a two-channel Agilent 81110 A pulse generator with adjustable rise/fall times (2 ns–10 ms). The circuit's resistor-capacitor (*RC*) time constant can be adjusted using an in-series resistance of $R = 100\,\Omega$–$1\,\mathrm{M}\Omega$. For fatigue testing, bipolar square pulses with identical rise/fall times of 2 ns were supplied by the pulse generator with voltage/duration characteristics of ±4 V/500 ns at a repetition frequency of 1 MHz.

First-principles calculations

The distributions of the oxygen vacancies over the thicknesses of the amorphous and crystalline HZO structures after ion implantation were obtained through an SRIM simulation using the parameters that are listed in Supplementary Table S1. In general, the light F and O ions that are present during dry etching using SF_6 and O_2 gases can collide effectively with the elements of HZO and create defects (e.g., oxygen, hafnium, and/or zirconium vacancies) (see Supplementary Fig. S1c)[52]. The oxygen moving and ferroelectric displacement barriers for specific distributions of the oxygen vacancies within the *O*-phase grains were calculated from the MEP using the nudged elastic band (NEB) method[53]. A series of intermediate states were generated between the initial and final state structures by linear interpolation, and the MEP was obtained when the joint action of the potential energy and the spring force for all intermediate state structures converged. The entire NEB process relies on the Vienna Ab initio Simulation Package. Throughout the calculations, the Perdew-Burke-Ernzerhof for Solid function functional was used, and the energy cutoff was set at 520 eV[54]. To ensure computational precision, a 2 × 2 × 2 Monkhorst-Pack *k*-point grid was implemented in the calculations.

Data availability

Source data are provided in this paper.

Code availability

Supplementary code is provided with this paper.

References

1. Ribes, G. et al. Review on high-k dielectrics reliability issues. *IEEE T. Device Mat. Reliab.* **5**, 5–19 (2005).
2. Cao, W. et al. The future transistors. *Nature* **620**, 501–515 (2023).
3. Kim, J. et al. Ultrahigh capacitive energy density in ion-bombarded relaxor ferroelectric films. *Science* **369**, 81–84 (2020).
4. Pan, H. et al. Ultrahigh energy storage in superparaelectric relaxor ferroelectrics. *Science* **374**, 100–104 (2021).
5. Stengel, M., Vanderbilt, D. & Spaldin, N. A. Enhancement of ferroelectricity at metal–oxide interfaces. *Nat. Mater.* **8**, 392–397 (2009).
6. Stengel, M. & Spaldin, N. A. Origin of the dielectric dead layer in nanoscale capacitors. *Nature* **443**, 679–682 (2006).
7. Sirenko, A. A. et al. Soft-mode hardening in $SrTiO_3$ thin films. *Nature* **404**, 373–376 (2000).
8. Hwang, C. S. Thickness-dependent dielectric constant of (Ba,Sr) TiO_3 thin films with Pt or conducting oxide electrodes. *J. Appl. Phys.* **92**, 432–437 (2002).
9. Sinnamon, L. J., Bowman, R. M. & Gregg, J. M. Investigation of dead-layer thickness in $SrRuO_3/Ba_{0.5}Sr_{0.5}TiO_3/Au$ thin-film capacitors. *Appl. Phys. Lett.* **78**, 1724–1726 (2001).
10. Mead, C. A. Anomalous capacitance of the thin dielectric structures. *Phys. Rev. Lett.* **6**, 545–546 (1961).
11. Saad, M. M. et al. Intrinsic dielectric response in ferroelectric nano-capacitors. *J. Phys. Condens. Matter.* **16**, L451–L456 (2004).
12. Junquera, J. & Ghosez, P. Critical thickness for ferroelectricity in perovskite ultrathin films. *Nature* **422**, 506–509 (2003).
13. Cheema, S. S. et al. Ultrathin ferroic HfO_2–ZrO_2 superlattice gate stack for advanced transistors. *Nature* **604**, 65–71 (2022).
14. Tomida, K., Kita, K. & Toriumi, A. Dielectric constant enhancement due to Si incorporation into HfO_2. *Appl. Phys. Lett.* **89**, 142902 (2006).
15. Yun, Y. et al. Intrinsic ferroelectricity in Y-doped HfO_2 thin films. *Nat. Mater.* **21**, 903–909 (2022).
16. Müller, J. et al. Ferroelectricity in yttrium-doped hafnium oxide. *J. Appl. Phys.* **110**, 114113 (2011).
17. Böscke, T. S., Müller, J., Bräuhaus, D., Schröder, U. & Böttger, U. Ferroelectricity in hafnium oxide thin films. *Appl. Phys. Lett.* **99**, 102903 (2011).
18. Polakowski, P. & Müller, J. Ferroelectricity in undoped hafnium oxide. *Appl. Phys. Lett.* **106**, 232905 (2015).
19. Martin, D. et al. Downscaling ferroelectric field effect transistors by using ferroelectric Si-doped HfO_2. *Solid-State Electron* **88**, 65–68 (2013).
20. Cheema, S. S. et al. Enhanced ferroelectricity in ultrathin films grown directly on silicon. *Nature* **580**, 478–482 (2020).
21. Watanabe, Y. et al. Achievement of higher-k and high-Φ in phase controlled HfO_2 film using post gate electrode deposition annealing. *ECS Trans.* **11**, 35 (2007).
22. Shelby, S. et al. Origin of ferroelectric phase stabilization via the clamping effect in ferroelectric hafnium zirconium oxide thin films. *Adv. Electron. Mater.* **8**, 2200601 (2022).
23. Kim, S. K. & Mihaela, P. Future of dynamic random-access memory as main memory. *MRS Bull.* **43**, 334–339 (2018).
24. Luo, Q. et al. A highly CMOS compatible hafnia-based ferroelectric diode. *Nat. Commun.* **11**, 1391 (2020).
25. Chen, Y.-H. et al. Enhanced sub 20-nm FinFET performance by stacked gate dielectric with less oxygen vacancies featuring higher current drive capability and superior reliability. 2015 IEEE International Electron Devices Meeting (IEDM), 21.3.1–21.3.4 (2015).
26. Walters, G., Shekhawat, A., Moghaddam, S., Jones, J. L. & Nishida, T. Effect of in situ hydrogen plasma on the ferroelectricity of hafnium zirconium oxide films. *Appl. Phys. Lett.* **116**, 032901 (2020).
27. Chen, K., Chen, P., Kao, R., Lin, Y. & Wu, Y. Impact of plasma treatment on reliability performance for $HfZrO_x$-based metal-ferroelectric-metal capacitors. *IEEE Electr. Device Lett.* **39**, 87–90 (2018).
28. Kang, K. et al. Highly enhanced ferroelectricity in HfO_2-based ferroelectric thin film by light ion bombardment. *Science* **376**, 731–738 (2022).
29. Cheema, S. S. et al. Giant energy storage and power density negative capacitance superlattices. *Nature* **629**, 803–809 (2024).
30. Glinchuk, M. D. et al. Possible electrochemical origin of ferroelectricity in HfO_2 thin films. *J. Alloy. Compd.* **830**, 153628 (2020).
31. Wei, W. et al. Spontaneous polarization enhancement in ferroelectric $Hf_{0.5}Zr_{0.5}O_2$ using atomic oxygen defects engineering: an ab initio study. *Appl. Phys. Lett.* **115**, 092905 (2019).
32. Kulikov, A. G. et al. Variation of a defect structure of lithium tetraborate ($Li_2B_4O_7$) in an external electric field. *Phys. Solid State* **61**, 548–554 (2019).
33. Luo, C. T. et al. Phase coexistence and transformations in field-cooled ternary piezoelectric single crystals near the morphotropic phase boundary. *Appl. Phys. Lett.* **105**, 232901 (2014).
34. Talanov, M. V., Bush, A. A., Sirotinkin, V. P. & Kozlov, V. I. Structural origin of strongly diffused ferroelectric phase transition in Ba(Ti, Zr) O_3-based ceramics. *Acta Mater.* **227**, 117734 (2022).
35. Jonscher, A. K. Dielectric relaxation in solids. Chelsea Dielectrics Press, pp. 62–101 (1983).
36. Dawber, M., Jung, D. J. & Scott, J. F. Perimeter effect in very small ferroelectrics. *Appl. Phys. Lett.* **82**, 436–438 (2003).
37. Jung, D. J. et al. Effect of microgeometry on switching and transport in lead zirconate titanate capacitors: implications for etching of nano-ferroelectrics. *J. Appl. Phys.* **95**, 4968–4975 (2004).
38. Gartena, L. M. & Trolier-McKinstry, S. The field induced $e_{31,f}$ piezoelectric and Rayleigh response in barium strontium titanate thin films. *Appl. Phys. Lett.* **105**, 132905 (2014).
39. Filipic, C., Levstik, A. & Kutnjak, Z. Analytical behaviour of dielectric nonlinearity in $PbMg_{1/3}Nb_{2/3}O_3$ relaxor ferroelectric. *Ferroelectrics* **257**, 63–68 (2001).
40. Viehland, D., Jang, S. J. & Cross, L.E. Freezing of the polarization fluctuations in lead magnesium niobate relaxors. *J. Appl. Phys.* **68**, 2916 (1990).
41. Zhou, D. Y. et al. Wake-up effects in Si-doped hafnium oxide ferroelectric thin films. *Appl. Phys. Lett.* **103**, 192904 (2013).
42. Jiang, A. Q., Lin, Y. Y. & Tang, T. A. The growth of interfacial-passive layers under thermal passivation of integrated $Pb(Zr,Ti)O_3$ thin films. *J. Appl. Phys.* **102**, 074118 (2007).
43. Scott, J. F. & Dawber, M. Oxygen-vacancy ordering as a fatigue mechanism in perovskite ferroelectrics. *Appl. Phys. Lett.* **76**, 3801–3803 (2000).
44. Wei, J. C., Jiang, L. L., Huang, M. L., Wu, Y. N. & Chen, S. Y. Intrinsic defect limit to the growth of orthorhombic HfO_2 and $(Hf,Zr)O_2$ with strong ferroelectricity: first-principles insights. *Adv. Funct. Mater.* **31**, 2104913 (2021).
45. Huan, T. D. et al. Pathways towards ferroelectricity in hafnia. *Phys. Rev. B* **90**, 064111 (2014).
46. Park, M. H. et al. Evolution of phases and ferroelectric properties of thin $Hf_{0.5}Zr_{0.5}O_2$ films according to the thickness and annealing temperature. *Appl. Phys. Lett.* **102**, 242905 (2013).
47. Materlik, R., Künneth, C. & Kersch, A. The origin of ferroelectricity in $Hf_{1-x}Zr_xO_2$: a computational investigation and a surface energy model. *J. Appl. Phys.* **117**, 134109 (2015).
48. Zhao, X. & Vanderbilt, D. First-principles study of structural, vibrational, and lattice dielectric properties of hafnium oxide. *Phys. Rev. B* **65**, 233106 (2002).
49. Adelmann, C. et al. Atomic layer deposition of Gd-doped HfO_2 thin films. *J. Electrochem. Soc.* **157**, G105–G110 (2010).
50. Hamouda, W. et al. Physical chemistry of the $TiN/Hf_{0.5}Zr_{0.5}O_2$ interface. *J. Appl. Phys.* **127**, 064105 (2020).

51. Jiang, A. Q., Liu, X. B. & Zhang, Q. Nanosecond-range imprint and retention characterized from polarization-voltage hysteresis loops in insulating or leaky ferroelectric thin films. *Appl. Phys. Lett.* **99**, 142905 (2011).
52. Moreira, P. A. F. P. et al. Molecular-dynamics simulation of threshold displacement energies in zircon. *Nucl. Instrum. Methods Phys. Res. Sect. B: Beam Interact. Mater. At.* **267**, 3431–3436 (2009).
53. Jónsson, H., Mills, G. & Jacobsen, K. W. Nudged elastic band method for finding minimum energy paths of transitions. In: *Classical and quantum dynamics in condensed phase simulations* 385–404 (1998).
54. Perdew, J. P. et al. Restoring the density-gradient expansion for exchange in solids and surfaces. *Phys. Rev. Lett.* **100**, 136406 (2008).
55. Luo, Z. et al. 5.1 Å EOT and low leakage TiN/Al_2O_3/$Hf_{0.5}Zr_{0.5}O_2$/Al_2O_3/TiN heterostructure for DRAM capacitor. *Appl. Phys. Lett.* **122**, 192903 (2023).
56. Zhou, J. R. et al. Al-doped and deposition temperature-engineered HfO_2 near morphotropic phase boundary with record dielectric permittivity (~68). *In*: 2021 IEEE International Electron Devices Meeting (IEDM), 13–14 (2021).
57. Wang, Y. et al. A stable rhombohedral phase in ferroelectric $Hf(Zr)_{1+x}O_2$ capacitor with ultralow coercive field. *Science* **381**, 558–563 (2023).
58. Park, M. H. et al. Ferroelectricity and antiferroelectricity of doped thin HfO_2-based films. *Adv. Mater.* **27**, 1811–1831 (2015).
59. Oh, S., Jang, H. & Hwang, H. Accurate evaluation of high-k HZO/ZrO_2 films by morphotropic phase boundary. *IEEE Electr. Device Lett.* **45**, 28–31 (2023).

Acknowledgements

This work was supported by the National Key Basic Research Program of China (grant number 2022YFA1402904), the National Natural Science Youth Foundation of China (grant number 12204393), the National Natural Science Foundation of China (grant number 62174034), Shanghai Center of Brain-inspired Intelligent Materials and Devices (ZJ2022-ZD-007), the Research Grant Council of Hong Kong Special Administrative Region China (Project No. PolyU25300022), and the Department of Science and Technology of Guangdong Province (grant number 2024A1515012752). Z.B.C. would also like to express his sincere thanks for the financial support from the Research Office (Project Code: P0042733 and P0039581) of The Hong Kong Polytechnic University. We thank professor Yingguo Yang and Zongquan Gu at Fudan University to provide the facilities for the XRD characterization, and David MacDonald, MSc, from Liwen Bianji (Edanz) (www.liwenbianji.cn/) for editing the English text of a draft of this manuscript.

Author contributions

A.Q.J. conceived the idea for the work, performed the electrical characterization, and wrote the manuscript. Z.B.C. supervised the microstructural characterizations and revised the manuscript. W.D.Z carried out the device fabrication, SEM imaging, XRR, and XRD measurements with the aid of B.L, Z.Z.S., Z.B.C., and Y.C. performed the TEM observations. S.Q.T., J.C.W., and S.Y.C. performed SRIM and first-principles calculations. All authors discussed the results.

Competing interests

The authors declare no competing interests.

Additional information

Supplementary information The online version contains supplementary material available at https://doi.org/10.1038/s41467-025-57963-8.

Correspondence and requests for materials should be addressed to Shi You Chen, Zi Bin Chen or An Quan Jiang.

Peer review information *Nature Communications* thanks Anna G. Chernikova, and the other, anonymous, reviewer(s) for their contribution to the peer review of this work. A peer review file is available.